

Parity-violating Electron Scattering and the Electric and Magnetic Strange Form Factors of the Nucleon

D. S. ARMSTRONG

Department of Physics, College of William and Mary, Williamsburg, VA 23187

R. D. McKEOWN

Thomas Jefferson National Accelerator Facility, Newport News, VA 23606;

Department of Physics, College of William and Mary, Williamsburg, VA 23187

Key Words neutral current, lepton scattering, electromagnetic form factors, strange form factors

Abstract Measurement of the neutral weak vector form factors of the nucleon provides unique access to the strange quark content of the nucleon. These form factors can be studied using parity-violating electron scattering. A comprehensive program of experiments has been performed at three accelerator laboratories to determine the role of strange quarks in the electromagnetic form factors of the nucleon. This article reviews the remarkable technical progress associated with this program, describes the various methods used in the different experiments, and summarizes the physics results along with recent theoretical calculations.

CONTENTS

INTRODUCTION	2
STRANGE QUARKS IN THE NUCLEON	2
NEUTRAL WEAK FORM FACTORS	4
<i>Radiative corrections</i>	6
<i>Axial Form Factor Corrections</i>	6
PARITY-VIOLATING ELECTRON SCATTERING	7
<i>Theory</i>	7
<i>Experimental Technique</i>	10
EXPERIMENTAL RESULTS	13
<i>SAMPLE</i>	13
<i>HAPPEX</i>	15
<i>G⁰</i>	16
<i>PVA4</i>	17
CONCLUSIONS	18

ACKNOWLEDGEMENTS	19
NUMBERED LITERATURE CITED	19

1 INTRODUCTION

Since the initial development of QCD in the 1970's, it has been known that the internal structure of the nucleon is due to the presence of quarks, gluons, and a "sea" of quark-antiquark pairs. Although the electric charge of the nucleon is due to the valence quarks (as in the early quark models of Gell-Mann and Zweig), in QCD the gluons are critical to quark confinement, generating 98% of the nucleon mass in the process. The results of polarized deep inelastic scattering experiments in the 1980's and 1990's indicated that, contrary to theoretical expectations, the spin of the nucleon does not arise from the spins of the quarks. As a result, the role of the gluons and the quark-antiquark pairs in the static properties of the nucleon became a subject of great interest. Although the gluons are responsible for dramatic effects like confinement and nucleon mass, the effects of the quark-antiquark pairs (necessarily generated by the gluons in QCD and therefore non-zero) are more difficult to ascertain. One can think of this as the QCD analog of the famous Lamb shift in atomic physics.

The strange quark-antiquark pairs are of particular interest, since there are no valence strange quarks in the nucleon and any process sensitive to strange quarks would necessarily be related to the "sea". In 1988, Kaplan and Manohar (1) proposed the study of study of strange quark-antiquark pairs by measurements of neutral weak current matrix elements, perhaps in neutrino scattering experiments. In 1989, McKeown (2) and Beck (3) proposed that parity-violating electron scattering offered a very effective method to study these matrix elements, generating significant interest and many new experimental proposals. In the subsequent two decades a great deal of experimental and theoretical effort resulted in a now rather definitive body of work that, for the first time, substantially constrains the contribution of strange quark-antiquark pairs to the elastic electroweak form factors of the nucleon.

2 STRANGE QUARKS IN THE NUCLEON

The most direct evidence for the existence of quarks and antiquarks in the nucleon is obtained from deep-inelastic lepton scattering. In this process a high momentum virtual photon interacts with the fundamental charges in the nucleon (quarks and antiquarks). Through the study of lepton-proton and lepton-neutron scattering, and using charge symmetry (with approximate treatment of charge symmetry breaking effects) one can extract information related to the probability distributions for up, down, and sea quarks. These distributions, known as parton distribution functions (PDF), are defined as a function of momentum fraction in the nucleon, x ($0 < x < 1$), and are denoted $q(x)$ and $\bar{q}(x)$, where $q = u, d, c, s, t, b$ for the quark flavors. In addition, the production of like-sign dimuon pairs in deep-inelastic charged-current neutrino scattering provides information on the strange quark distribution. Another important ingredient in the flavor decomposition of the sea quarks is provided by Drell-Yan experimental data, in which an incident quark (in the projectile nucleon) annihilates on an antiquark (in the target nucleon) producing a $\mu^+\mu^-$ pair. Recent Drell-Yan data

on the proton and deuteron have been combined to indicate a startling excess of $\bar{d}(x)/\bar{u}(x)$. Finally, the evolution of the quark and antiquark PDF's as a function of Q^2 provides information on the gluon PDF $g(x)$. Fig. 1 shows the results of the PDF's obtained in a recent global fit to deep inelastic scattering and Drell-Yan data.

The general features of the PDF's shown in Fig. 1 are qualitatively well understood. The dominance of u and d at higher $x > 0.1$ indicates the valence nature of these quark flavors (three valence quarks, each with average $x \sim 1/3$). The dramatic rise of $g(x)$ at low x is associated with the "splitting" of partons at lower x , e.g., $q(x) \rightarrow q(y) + g(x-y)$. The sea quarks arise from $\bar{q}q$ pair production by gluons via $g(x) \rightarrow q(y) + \bar{q}(x-y)$. Thus one can infer that the gluons dominate the dynamics at low x and the presence of the sea quarks is a secondary feature of the presence of the large number density of gluons.

However, there is a very interesting and important effect at intermediate x ($0.01 < x < 0.1$) where (due to the Drell-Yan data discussed above) one finds a substantial excess of $\bar{d}(x)$ relative to $\bar{u}(x)$. Clearly the process $g \rightarrow \bar{q}q$ would produce $\bar{u} = \bar{d}$ (except for small effects due to $m_u \neq m_d$). The $\bar{d}(x)/\bar{u}(x)$ excess must then be attributed to non-perturbative processes. For example, the fluctuation of a proton into a neutron and π^+ contains a \bar{d} component and there is no symmetric analog process to produce \bar{u} . (Note that $p \rightarrow p\pi^0$ produces equal numbers of \bar{u} and \bar{d}). In addition, one would expect that the \bar{d} excess from this process would occur at the value $x \sim m_\pi/(2m_N)$, in agreement with the experimental data. Thus this observed excess of $\bar{d}(x)/\bar{u}(x)$ strongly indicates the presence of fluctuations into $N\pi$ pairs in the nucleon. Of course, many models of the nucleon (such as the "cloudy bag" models) include such configurations in an attempt to capture the physics associated with other observables (such as the anomalous magnetic moments).

Thus one is naturally led to consider the possible role of similar fluctuations such as $p \rightarrow K^+\Lambda$. Clearly such configurations will have lower probability than $N\pi$ fluctuations due to the higher masses of the Λ and K^+ , but one would certainly expect there to be finite observable effects resulting from them. Such configurations would lead to radially separated distributions of \bar{s} and s quarks, due to the tendency of the K^+ to occupy larger radial distances from the center of mass of the ΛK^+ . The spatial separation of the s and \bar{s} would have several implications:

1. $\bar{s}s$ contribution to the nucleon magnetic moment, and other electroweak form factors,
2. $\bar{s}s$ contribution to the nucleon axial charge, affecting the value of Σ associated with the helicity carried by quarks,
3. $\bar{s}s$ contribution to the mass of the nucleon,
4. difference between the PDF's $s(x)$ and $\bar{s}(x)$.

The first three of these items are low Q^2 or static properties of the nucleon. Thus they represent a change in the nucleon static properties analogous to the change in atomic properties (e.g. the Lamb shift) due to vacuum polarization in QED. The fourth item is an effect analogous to the $\bar{d}(x)/\bar{u}(x)$ excess observed in the Drell-Yan process. In principle, items 1.) and 4.) can be established in a model-independent fashion, whereas the items 2.) and 3.) generally require a model-dependent analysis or assumptions about non-perturbative QCD effects.

At present, although there have been many hints of effects associated with items 2-3.) there is no unassailable demonstration that the evidence can be due to the strange quark effects. For item 4.), there is only a hint in the latest global PDF fit, MSTW08 (4), as shown in Fig. 2.

For the remainder of this review, we will focus on the theoretical framework, experimental techniques, and experimental results associated with the studies of $\bar{s}s$ contribution to the nucleon magnetic moment, and other electroweak form factors (item 1.) above).

3 NEUTRAL WEAK FORM FACTORS

The elastic scattering of nucleons via the neutral weak current can be described by two vector form factors, F_1^Z and F_2^Z , and an axial vector form factor G^Z . These form factors are functions of the invariant momentum transfer Q^2 . Like the electromagnetic interaction, the neutral weak interaction with a nucleon involves coupling to the quarks (and antiquarks) as the gluons have no electroweak interaction. In general, we can write any of the elastic electroweak form factors in terms of the quark flavors. For example the electromagnetic form factors are given by

$$F_1^\gamma = \frac{2}{3}F_1^u - \frac{1}{3}F_1^d - \frac{1}{3}F_1^s \quad (1)$$

$$F_2^\gamma = \frac{2}{3}F_2^u - \frac{1}{3}F_2^d - \frac{1}{3}F_2^s \quad (2)$$

where u , d , and s refer to the up, down and strange quarks. Note that we ignore charm and heavier quarks as it has been shown that these can be safely neglected. The neutral weak form factors may be also written in terms of the individual quark flavor components

$$F_{1,2}^Z = (1 - \frac{8}{3}\sin^2\theta_W)F_{1,2}^u + (-1 + \frac{4}{3}\sin^2\theta_W)(F_{1,2}^d + F_{1,2}^s) \quad (3)$$

$$G_A^Z = -G_A^u + G_A^d + G_A^s \quad (4)$$

where θ_W is the weak mixing angle. The value of θ_W is, in principle, precisely determined from other experiments (5) although one must consider the renormalization scheme and radiative corrections.

For the vector form factors, one often prefers to use the Sachs form factors

$$\begin{aligned} G_E^{\gamma,Z} &= F_1^{\gamma,Z} - \tau F_2^{\gamma,Z} \\ G_M^{\gamma,Z} &= F_1^{\gamma,Z} + F_2^{\gamma,Z} \end{aligned} \quad (5)$$

with $\tau \equiv Q^2/4M^2$. In the static limit, the electromagnetic form factors then reduce to the charge and magnetic moment: $G_E^\gamma(Q^2 = 0) = Q$ and $G_M^\gamma(Q^2 = 0) = \mu$. Another useful quantity is the charge radius:

$$\langle r^2 \rangle = -6 \left. \frac{dG_E(Q^2)}{dQ^2} \right|_{Q^2=0}. \quad (6)$$

Assuming isospin symmetry, additional relations among the form factors are obtained using the fact that the transformation of proton to neutron ($p \rightarrow n$) is

equivalent to changing u to d and vice versa ($u \leftrightarrow d$). For example, the proton and neutron axial form factors are then related to the quark components (defined for the proton) by

$$G_A^{Z,p} = -G_A^u + G_A^d + G_A^s \quad (7)$$

$$G_A^{Z,n} = -G_A^d + G_A^u + G_A^s. \quad (8)$$

One can then isolate the strange axial form factor by

$$G_A^s = \frac{(G_A^{Z,p} + G_A^{Z,n})}{2}. \quad (9)$$

In principle, this would be a way to access the matrix element $G_A^s(Q^2 = 0) = \langle \bar{s} \gamma^\mu \gamma_5 s \rangle S_\mu$, where S is the nucleon spin four-vector. Again, in practice one must consider radiative corrections and, for this axial form factor, the contribution of anapole effects as discussed in 3.2 below. The theoretical uncertainties associated with these corrections render measurement of the strange contribution Δs problematic in parity violating electron scattering.

For the vector form factors, the use of isospin symmetry yields the important relation

$$G_{E,M}^{Z,p} = (1 - 4 \sin^2 \theta_W) G_{E,M}^{\gamma,p} - G_{E,M}^{\gamma,n} - G_{E,M}^s \quad (10)$$

which illustrates how measurement of the electromagnetic form factors for the proton and neutron, combined with measurement of the corresponding $G^{Z,p}$, can provide access to the strange vector form factors. In this case, as discussed in 3.1, the radiative corrections are manageable and parity-violating electron scattering is a very useful tool for studying strange vector form factors. In the static limit, one has the particularly interesting quantity $\mu_s \equiv G_M^s(Q^2 = 0)$ known as the strange magnetic moment. Since the net strangeness in the nucleon is zero, one has $G_E^s(Q^2 = 0) = 0$. However, the mean squared strangeness radius $r_s^2 \equiv -6[dG_E/dQ^2](Q^2 = 0)$ is a static property that in general can be non-zero.

Over the last 2 decades, there have been numerous theoretical papers reporting predictions for strange vector form factors. Most of these papers involve models of nucleon structure which, although well-motivated, involve many uncertainties related to the expected accuracy of the predictions. A good review of the model calculations can be found in (6). Many of the models predict values for μ_s and the results generally range from $-0.5 < \mu_s < 0.3$ n.m., with a strong preference for negative values. The predicted values for r_s also cover a substantial range $-0.25 < r_s < 0.4$ fm.

In the last few years, calculations based on input from lattice QCD methods have become available. The challenge associated with lattice calculations involves the evaluation of so-called “disconnected” insertions, where the vector current couples to a quark loop that does not involve the valence quarks. (Since there are no valence strange quarks, these are the amplitudes relevant to strange form factors). In one approach (7), the baryon octet matrix elements are written with connected and disconnected insertions in separate terms. Linear combinations of the baryon magnetic moments are used, along with the assumption of charge symmetry, to obtain expressions involving the baryon magnetic moments and ratios of amplitudes to be evaluated using lattice calculations. It is claimed that the ratios are reliably determined from lattice calculations, and this method yields the prediction $\mu_s = -0.046 \pm 0.019$ n.m., with the uncertainty estimated from the

lattice statistical precision. A similar approach (8) was then used to compute the strange radius $r_s^2 = 0.021 \pm 0.063 \text{ fm}^2$, where the uncertainty is predominantly due to the poor experimental information on baryon charge radii.

More recently, a more direct approach (9) using lattice methods has been employed. Using a full QCD calculation using $N_f = 2 + 1$ clover fermion configurations the result $\mu_s = -0.017 \pm 0.025 \pm 0.07 \text{ n.m.}$ is obtained, where the first uncertainty is statistical and the second is due to uncertainties in Q^2 and chiral extrapolations. This result is in remarkable agreement with the more phenomenological result (7).

3.1 Radiative corrections

In order to extract contributions of strange form factors G^s from measurements of electroweak form factors, one must include the effects of $\mathcal{O}(\alpha)$ electroweak radiative corrections. These radiative effects typically arise from $\gamma - Z$ “box” diagrams or loop effects. It is common to express these $\mathcal{O}(\alpha)$ corrections as ratios $R_{V,A}$ (for vector V and axial vector A) which are fractions of the corresponding tree-level amplitudes. $R_V^p, R_V^n, R_V^{(0)}$ denote the ratios for vector proton, neutron, and SU(3)-singlet amplitudes, respectively. In principle, their values can be obtained using the Standard Model predictions for the effective electron-quark couplings C_{1q} given in (5). However, these C_{1q} do not include perturbative QCD contributions, nor coherent strong interaction effects in the radiative corrections associated with elastic scattering from a nucleon. A recent analysis of these effects has been given in Ref. (10) and up-dated in Ref. (11) (which also includes an improved treatment of strong interaction contributions to the running of the weak mixing angle in the \overline{MS} renormalization scheme from its value at the Z -pole) with the results

$$R_V^p = -0.0520 \quad (11)$$

$$R_V^n = -0.0123 \quad (12)$$

$$R_V^{(0)} = -0.0123. \quad (13)$$

The theoretical uncertainties in R_V^n and $R_V^{(0)}$ are less than one percent, while the theoretical uncertainty in $(1 - 4 \sin^2 \theta_W)(1 + R_V^p)$ is ± 0.0008 (11), or slightly more than one percent. (Since this error receives roughly equal contributions from the uncertainty in $\sin^2 \hat{\theta}_W(M_Z)$ as determined at the Z -pole and from the $\mathcal{O}(\alpha)$ $Z\gamma$ box graph corrections, it is not appropriate to quote an uncertainty in R_V^p alone.) For the range of Q^2 associated with the experiments discussed in this review, the R_V have a negligible impact on the Q^2 -dependence of A_{PV}^p and are taken to be constant. We adopt the conventional \overline{MS} renormalization scheme so that $\sin^2 \hat{\theta}_W$ is evaluated as $\sin^2 \hat{\theta}_W(M_Z) = 0.23116 \pm 0.00013$ (5).

3.2 Axial Form Factor Corrections

For the axial form factor, it is useful to employ the notation G_A^e to differentiate the quantity relevant to parity-violating electron scattering from other axial form factors (i.e., charged current processes or neutrino scattering). At lowest order this axial form factor is the same as G_A as measured in charged current processes [$G_A(Q^2 = 0) = -1.2701 \pm 0.0025$] (5). However, the presence of strange quarks

(i.e., the contribution Δs) and radiative effects must be included, and can be expressed

$$G_A^e(Q^2) = G_D(Q^2) \times [G_A(1 + R_A^{T=1}) + \frac{3F - D}{2} R_A^{T=0} + \Delta s(1 + R_A^{(0)})], \quad (14)$$

where

$$G_D(Q^2) = \frac{1}{(1 + Q^2/M_A^2)^2}, \quad (15)$$

parameterizes the Q^2 -dependence with a dipole form with the squared axial mass $M_A^2 = 1.00 \pm 0.04 \text{ GeV}^2$ (12). F and D are the octet baryon beta-decay parameters, which are determined from neutron and hyperon beta decays under the assumption of SU(3) flavor symmetry ($3F - D = 0.58 \pm 0.12$ (13)). $\Delta s = -0.07 \pm 0.06$ (14) is the strange quark contribution to nucleon spin obtained from inclusive polarized deep-inelastic lepton-nucleon scattering.

The ratios $R_A^{T=1}$, $R_A^{T=0}$, and $R_A^{(0)}$ characterize the effect of electroweak radiative corrections to the isovector, isoscalar, and SU(3) singlet components of the axial form factor. These quantities are traditionally divided into “one-quark” and “many-quark” contributions. The one-quark contributions correspond to renormalization of the effective vector electron-axial vector quark couplings, C_{2q} , and their values can be obtained from the Standard Model predictions for these couplings given in Ref. (5). The many-quark contributions include the so-called “anapole” effects as well as coherent strong interaction contributions to the radiative corrections. In contrast to the vector corrections, R_V , the *relative* importance of many-quark effects in the R_A can be quite pronounced. The many-quark effects can be addressed using chiral perturbation theory, and a comprehensive analysis of the anapole contributions to $R_A^{T=1}$ and $R_A^{T=0}$ has been carried out to chiral order p^3 in Ref. (15). The total axial corrections, up-dated for the present value of the weak mixing angle, are

$$R_A^{T=1} = -0.258 \pm 0.34 \quad (16)$$

$$R_A^{T=0} = -0.239 \pm 0.20 \quad (17)$$

$$R_A^{(0)} = -0.55 \pm 0.55. \quad (18)$$

4 PARITY-VIOLATING ELECTRON SCATTERING

4.1 Theory

The scattering of an electron from a hadronic target involves the dominant electromagnetic amplitude due to photon exchange \mathcal{M}_γ and the much smaller (at low momentum transfer $Q^2 \ll M_Z^2$) neutral weak amplitude due to Z exchange \mathcal{M}_Z . The scattering cross section is related to the squared modulus of the sum of these amplitudes $|\mathcal{M}_\gamma + \mathcal{M}_Z|^2$. Parity-violating observables arise from the fact that the weak amplitude involves both vector and axial vector currents, leading to pseudoscalar quantities. The incident electron helicity, $\hat{s} \cdot \hat{k}$, is a pseudoscalar quantity and so the helicity dependence of the cross section violates parity symmetry and must involve the weak amplitude. To lowest order, one expects the difference between positive helicity and negative helicity cross sections to depend

upon the product $d\sigma_R - d\sigma_L \propto \text{Re}[\mathcal{M}_\gamma \mathcal{M}_Z^{VA}]$, where \mathcal{M}_Z^{VA} is the weak amplitude associated with the product of vector and axial vector currents. The helicity independent cross section is just due to the dominant photon exchange amplitude $d\sigma_R + d\sigma_L \propto |\mathcal{M}_\gamma|^2$. Thus the parity-violating helicity-dependent asymmetry has the structure

$$A_{LR} \equiv \frac{d\sigma_R - d\sigma_L}{d\sigma_R + d\sigma_L} \quad (19)$$

$$\propto \frac{\text{Re}[\mathcal{M}_\gamma \mathcal{M}_Z^{VA}]}{|\mathcal{M}_\gamma|^2} \quad (20)$$

The squared electromagnetic amplitude must be proportional to $(e/Q^2)^4 = (4\pi\alpha/Q^2)^2$, whereas the product $\mathcal{M}_\gamma \mathcal{M}_Z^{VA}$ will be proportional to $(e/Q^2)^2 G_F/\sqrt{2} = 4\pi\alpha G_F/\sqrt{2}Q^2$. (At low Q^2 the weak amplitude involves the Fermi coupling constant $G_F = 1.16637 \times 10^{-5} \text{ GeV}^{-2}$.) Therefore, the parity-violating asymmetry can be written

$$A_{LR} = -\frac{G_F Q^2}{4\sqrt{2}\pi\alpha} \times \frac{\mathcal{N}}{\mathcal{D}} \quad (21)$$

in which the numerator \mathcal{N} involves products of electromagnetic and weak form factors and the denominator \mathcal{D} involves squares of electromagnetic form factors.

In lowest order, the expression for parity-violating electron nucleon scattering in the laboratory frame of reference (where the initial nucleon is at rest) is given by

$$A_{LR} \equiv \frac{d\sigma_R - d\sigma_L}{d\sigma_R + d\sigma_L} \quad (22)$$

$$= \left[\frac{-G_F Q^2}{4\sqrt{2}\pi\alpha} \right] \cdot (A_E + A_M + A_A) \quad (23)$$

where the three terms are

$$A_E = \frac{\epsilon G_E^\gamma G_E^Z}{\epsilon (G_E^\gamma)^2 + \tau (G_M^\gamma)^2} \quad (24)$$

$$A_M = \frac{\tau G_E^\gamma G_M^Z}{\epsilon (G_E^\gamma)^2 + \tau (G_M^\gamma)^2} \quad (25)$$

$$A_A = \frac{-\epsilon'(1 - 4\sin^2\theta_W)G_M^\gamma G_A^e}{\epsilon (G_E^\gamma)^2 + \tau (G_M^\gamma)^2}, \quad (26)$$

involving the kinematic variables

$$\begin{aligned} \tau &= \frac{Q^2}{4M_N^2} \\ \epsilon &= \frac{1}{1 + 2(1 + \tau) \tan^2 \frac{\theta}{2}} \\ \epsilon' &= \sqrt{\tau(1 + \tau)(1 - \epsilon^2)} \end{aligned} \quad (27)$$

which are functions of the momentum transfer $Q^2 = -q^2 > 0$ and the electron scattering angle θ . The different terms A_E , A_M and A_A depend upon the neutral weak form factors associated with the electric, magnetic, and axial couplings to

the nucleon and so provide access to the strange form factors G_E^s , G_M^s , and G_A^s , respectively. At small scattering angles, $\theta \rightarrow 0$ one finds that $\epsilon \rightarrow 1$, $\tau \rightarrow 0$, and $\epsilon' \rightarrow 0$, so A_E becomes the dominant term. At backward angles $\theta \rightarrow \pi$, $\epsilon \rightarrow 0$ and the asymmetry is dominated by the magnetic and axial asymmetries. Note also that the axial asymmetry is suppressed by the factor $(1 - 4\sin^2\theta_W)$, but the actual numerical value is quite sensitive to radiative and anapole effects. As a result, the dependence of A_{LR} on G_A^s is quite small and so one uses G_A^s as determined from spin-dependent deep inelastic scattering. Thus, in the end, one can treat A_{LR} as a (linear) function of the vector strange form factors G_E^s and G_M^s .

By evaluating Eq. 23 in terms of the vector strange form factors and including radiative corrections, one can express the asymmetry as

$$A_{LR} = A_{nvs} + \eta_E G_E^s + \eta_M G_M^s, \quad (28)$$

where A_{nvs} is the ‘‘non-vector-strange’’ asymmetry (independent of G_E^s and G_M^s), and η_E and η_M are functions of kinematic quantities and nucleon electromagnetic form factors. For elastic scattering from the proton, one can measure the asymmetry at a variety of scattering angles and fixed momentum transfer (by also varying the incident beam energy) to obtain values for different linear combination of the strange vector form factors. This procedure (analogous to the ‘‘Rosenbluth’’ separation for determining form factors from cross section measurements) facilitates determination of both G_E^s and G_M^s .

Another technique for experimental measurement of G_E^s involves elastic scattering from ${}^4\text{He}$. The ${}^4\text{He}$ nucleus has spin $S = 0$ and isospin $I = 0$, so the magnetic and axial form factors vanish. The charge form factor for electromagnetic scattering from ${}^4\text{He}$ is proportional to the isoscalar combination $G_E^{\gamma,p} + G_E^{\gamma,n}$. Similarly, the neutral weak form factor is proportional to $G_E^{Z,p} + G_E^{Z,n}$. One can use Eq. 10 to obtain a relation between the electromagnetic form factor for ${}^4\text{He}$, $F^\gamma(Q^2)$, and the neutral weak form factor $F^Z(Q^2)$:

$$F^Z(Q^2) = -F^\gamma(Q^2) \times \left(4\sin^2\theta_W + \frac{2G_E^s}{G_E^{\gamma,p} + G_E^{\gamma,n}} \right) \quad (29)$$

which then yields the parity-violating asymmetry for elastic $e - {}^4\text{He}$ scattering:

$$A_{PV}^{He} = \frac{G_F Q^2}{4\pi\sqrt{2}\alpha} \times \left(4\sin^2\theta_W + \frac{2G_E^s}{G_E^p + G_E^n} \right). \quad (30)$$

One should keep in mind that radiative corrections, as discussed in 3.1 and 3.2, lead to minor modifications of Eq. 23 and Eq. 30 and must be included for any quantitative analysis.

Finally, we mention that quasielastic scattering from deuterium has been employed to study the axial form factor G_A^e . As mentioned previously, this is not useful for constraining G_A^s , but does provide a method to test the calculations of the radiative corrections and anapole contributions to G_A^e . In the static approximation, one can treat quasielastic scattering from deuterium as simply the sum of scattering from a free proton and a free neutron. In this case the parity

violating asymmetry has the form

$$A_d = -\frac{G_F Q^2}{4\sqrt{2}\pi\alpha} \times \frac{\mathcal{N}_n + \mathcal{N}_p}{\mathcal{D}_n + \mathcal{D}_p} \quad (31)$$

where \mathcal{N}_p (\mathcal{D}_p) and \mathcal{N}_n (\mathcal{D}_n) are the numerators (denominators) in Eq. 23 for the proton and neutron, respectively. The asymmetry again can be expressed as a sum of three terms $A_E + A_M + A_A$ corresponding to numerator expressions involving electric, magnetic, and axial weak form factors. At backward angles, the contribution of A_E is negligible. The strange magnetic form factor contribution to A_M is reduced, due to the combination $(G_M^{\gamma,p} + G_M^{\gamma,n})G_M^s$ and the small value of the nucleon isoscalar magnetic form factor, relative to the axial term A_A . Thus at backward angles the deuteron asymmetry, when combined with the proton asymmetry, can provide useful information on the isovector part of the weak axial form factor G_A^e . Again, it is important to include radiative corrections in any quantitative analysis. In addition, the nuclear effects associated with the binding of the two nucleons in deuterium must also be considered.

4.2 Experimental Technique

The requirement to precisely measure parity-violating asymmetries of the scale of a few parts per million (ppm) imposes several significant experimental challenges. High statistical precision demands long running time and high luminosity, implying high beam current and thick targets, as well as a highly-polarized beam. The beam polarization must be well-determined, requiring high-quality beam polarimetry. Backgrounds need to be well-separated from the elastic or quasi-elastic scattering events of interest, and any residual background contributions must be precisely corrected for. The beam helicity needs to be rapidly flipped (typically at about 30 Hz) to suppress the effect of slow changes in detector or beam properties. In the ideal case, no other beam property should change when the helicity is reversed. Fluctuations in beam properties such as intensity, trajectory, and energy that are correlated with the helicity “flip” must be minimized, and the sensitivity of the apparatus to such helicity-correlated changes needs to be determined, so that corrections can be made for the residual fluctuations. Additional slow flips of the beam helicity can then be made to suppress many remaining systematics. In this section we discuss several aspects of the various approaches adopted to meet these challenges.

4.2.1 POLARIZED ELECTRON SOURCE The need for a highly-polarized, high-current electron beam with exquisite stability under reversal of the helicity dictates that a key component of these experiments is the polarized electron source. The adopted technology, pioneered at SLAC in the 1970’s (16), is based on the emission of electrons from a GaAs photocathode when exposed to circularly-polarized laser light. Beam polarizations of near 40% and currents of up to 100 μ A were obtained using “bulk” GaAs crystals for the photocathode (17). Higher polarization (at the expense of high beam current) was subsequently produced using “strained” crystals, in which the active layer of the photocathode was a thin (\sim 100 nm) layer of GaAs grown on GaAsP (18). The mismatch between the two lattices produced a strain in the GaAs, breaking the degeneracy in its energy levels, theoretically allowing up to a 100% polarization (19,20). More

recently, the adoption of multi-layer “superlattice” crystals (21) has allowed both high polarization (89%) and high current (100 μA) (22).

4.2.2 BEAM MONITORING AND CONTROL High-precision parity-violation experiments impose stringent requirements on the polarized electron beam in order to minimize false asymmetries generated by helicity-correlated variations in beam properties. This demands careful attention to the optical properties of the incident laser light at the electron source.

The fast helicity reversal of the electron beam is accomplished by reversing the handedness of the laser light using a Pockels cell, which is a birefringent crystal whose indices of refraction change with the application of an electric field. Linearly polarized light from the source laser, with polarization at 45° to the transmission axes, acquires a phase shift between the components on the slow and fast axes; by adjusting the voltage one can convert the light to either right or left-handed circular polarization. Imperfections in the Pockels cell typically lead to a small residual component of linear polarization, which is different for the two nominal circular polarization states. The linear components are transported differently by the various optical elements, leading to helicity-correlated intensity variations. Gradients in the birefringence in the cell also generate helicity-correlated changes in the trajectory of the light, leading to electron beam position variations (23), which can also lead to intensity variations, as the quantum efficiency of the photocathode usually varies over its surface. The adoption of strained GaAs photocathodes makes these effects especially acute: the strain introduces an anisotropy in the quantum efficiency of the cathode, making it the dominant source of analyzing power in the system.

Various passive and active techniques have been adopted to suppress these helicity-correlated effects. Passive techniques include careful alignment of the laser beam through the Pockels cell (24), minimization of optically active elements in the laser path, and attention to optimum beam transport in the accelerator, to realize the natural “adiabatic damping” of position fluctuations in the acceleration process. Active techniques include feedback based on measurements of the helicity-correlated changes in beam intensity and position in the experimental hall.

Figure 4 depicts a typical polarized electron source setup, in this case the Jefferson Lab source as used in recent parity experiments (25, 26, 27, 28, 29). Two independent systems have been used to suppress the intensity variations. The first uses adjustment of the voltage signal to the Pockels cell - small differences in the voltages for the two helicity states modify the residual linear polarization of the transported light, leading to helicity-correlated intensity variations, which then can be adjusted. The second system, the IA (Intensity Attenuator), consists of a second Pockels cell and a waveplate (WP), sandwiched between two parallel linear polarizers (LP). This Pockels cell (PC) is operated at low helicity-dependent voltages (to minimize beam-steering effects) and acts as an electro-optic adjustable shutter. In either case, helicity-correlated electron beam intensity variations are measured, typically every few minutes, and a feedback signal is sent to the electron source to null the variations.

Both the SAMPLE experiment and forward-angle phase of the G0 experiment also used active feedback on helicity-correlated position differences in the beam (30). Here a piezoelectric-controlled steering mirror (see Fig. 4) is used to move the beam in a helicity-controlled manner.

Another technique is to use an insertable half-wave plate (IHWP) in the optical path, as shown in Fig. 4. The IHWP is periodically inserted or removed on a time scale of many hours. The IHWP rotates the linear polarization state by 90° , thereby inverting the sense of the resulting circular polarization with respect to the Pockels cell voltage. This slow “flip” should reverse the sign of the measured asymmetry in the Hall with respect to the helicity control signal, in the absence of any false asymmetry picked up in the experimental electronics due to the helicity-control signal. Many sources of helicity-correlated beam changes are insensitive to the state of the IHWP, and thus this flip cancels these systematics.

To ensure that there are no false asymmetries in the data due to the helicity-control signal being picked up by the experimental electronics, the fast helicity reversal follows a pseudorandom pattern, and the helicity state reported to the electronics is delayed by several states in the pattern, and only later reconstructed in software.

To illustrate the high suppression of helicity-correlated beam fluctuations afforded by these techniques, consider the HAPPEX-II measurement. Here the values for these variations, averaged over the entire several month-long run, were 0.4 ppm for intensity, < 1.7 nm for position, < 0.2 nrad for angle and 0.2 ppb for energy.

The sensitivity of the apparatus to these residual fluctuations can be determined either by multi-parameter linear regression of the natural fluctuations, or by taking subsets of the data with individual beam parameters modulated in a controlled manner (49).

4.2.3 BEAM POLARIMETRY Precision knowledge of the beam polarization is essential for normalizing the measured asymmetries. Various polarimeters have been adopted in these experiments, including those that measure continuously during the experiment, such as transmission (31, 32) and backscattering (33, 34, 35, 36, 37) Compton polarimeters, and those that are invasive, which can only make periodic measurements of the polarization, such as Mott (38) and Moller (39, 40, 41, 32) polarimeters. The highest precision reached to date was in the HAPPEX-III measurement, where a combination of Moller and backscattering Compton devices yielded a precision of 0.75% (22).

4.2.4 COUNTING VS. INTEGRATING METHODS FOR ASYMMETRY MEASUREMENTS Two approaches have been adopted for the measurement of the parity-violating asymmetry. The challenge is to accommodate the extremely high rates (of order 10 to 100 MHz) of scattered electrons that must be detected in order to achieve the desired statistical precision. One approach is a counting method, in which custom electronics are used to collect events in scalers (the G0 experiment) or energy histograms (the PVA4 experiment) which are accumulated for a given beam helicity state and then digitized at each helicity transition. In the other approach, the integrating method (SAMPLE and HAPPEX experiments), the analog signal from the detectors is integrated over a given helicity window and the integral is digitized at each helicity change. Challenges in the counting method include accounting for the effects of electronic deadtime and event pileup which can distort the measured asymmetry, as well as the design and cost of the custom electronics. In the integrating method one has to ensure a high degree of linearity of the entire electronics chain in order that helicity-correlated variations in the beam intensity not generate false asymmetries. In neither approach, unlike the usual nuclear physics experiment, can one digitize complete information

about individual scattering events, so only limited off-line analysis techniques for dealing with background processes are available.

4.2.5 TARGETS The program of parity-violating electron scattering experiments reviewed here generally involve the use of targets of hydrogen, deuterium and helium. The very small asymmetries to be measured imply that it is necessary to achieve high luminosity, so these targets must be cryogenic to achieve sufficient areal density. The use of cryogenic fluids introduces a new challenge: stability of the target density in the presence of the intense electron beam which causes thermal heating of the fluid. Thermal fluctuations are a potential source of additional noise that can degrade the statistical precision of the asymmetry measurement.

4.2.6 HYDROGEN AND DEUTERIUM TARGETS The operating point for a liquid hydrogen target is typically about 19 K, just a few degrees below the boiling point at a nominal pressure of 1-2 atm. Thus even with small temperature excursions the liquid remains significantly below the boiling point to minimize thermal fluctuations due to the beam. Indeed localized boiling, leading to bubble formation, is a major potential source of target thickness variations that can contribute significantly to statistical noise in the measured asymmetries. The fluid is generally pumped in a recirculation loop in order to constantly provide fresh liquid within the electron beam profile. The recirculation loop also contains a heat exchanger where heat is transferred to helium gas as the primary coolant. An ohmic heater in the loop is used to control the temperature and maintain the operating point by compensating for variations in the beam power. Safety is a major consideration in the design and operation of these targets, as a release of hydrogen gas to the room atmosphere can lead to a dangerous flammable mixture. Detailed descriptions of the SAMPLE (42), G0 (43) and PVA4 (44) targets are available in the literature.

4.2.7 HELIUM TARGETS One experiment, HAPPEX-Helium, adopted a high pressure ^4He gas target to directly measure the strange electric form factor G_E^s . The target was a 20-cm long cell maintained at a temperature and pressure of 7 K and 13 atm, in which the cryogenic ^4He was pumped through the cell in a direction transverse to the beam direction, so as to minimize local beam heating. Even without the possibility of bubble formation, beam-induced density fluctuations in the gas were a challenge, but were able to be limited to a few % increase in the statistical noise of the asymmetry measurement.

5 EXPERIMENTAL RESULTS

5.1 SAMPLE

The SAMPLE experiment, performed at the MIT-Bates Linear Accelerator Center, was primarily focused on the goal of determining the strange magnetic form factor G_M^s at low momentum transfer $Q^2 = 0.1 \text{ GeV}^2$. A rather complete description of the experiment and results can be found in (32), and we provide a short summary here. A 200 MeV polarized electron beam, typically 40 μA , was incident on a 40 cm long liquid hydrogen target. A schematic of the apparatus is shown in Fig. 5. The scattered electrons were detected in a large solid angle ($\sim 1.5 \text{ sr}$) air Cerenkov detector, with 10 ellipsoidal mirrors at backward angles $130^\circ < \theta < 170^\circ$, resulting in an average $Q^2 \simeq 0.1 \text{ (GeV}/c)^2$. At these kinematics

the axial term is expected to contribute about 20% of the asymmetry.

The hydrogen data set was acquired in 1998, and the experiment was run with a deuterium target in 1999 to acquire data on the axial form factor. The initial deuterium result indicated a substantial discrepancy with calculations of the axial form factor, and so further deuterium experiments at lower momentum transfer were performed in 2000-2001. These experiments, along with a reanalysis of the 1999 deuteron dataset (with improved accounting of pionic backgrounds) now provide significant confirmation of the theoretical treatment of the axial form factor.

The polarized electron source utilized bulk GaAs, with polarization typically about 35%. The Bates beam was pulsed at 600 Hz, and the beam helicity was changed for each pulse. A preselected random pattern of ten helicity states was generated, and the complement of this set (with reverse helicity) followed for the next ten pulses. The longitudinal spin emerging from the polarized source was pre-rotated by a Wien spin rotator before injection into the accelerator so the the 36.5° magnetic bend into the experimental hall would then provide longitudinal polarization at the target location. The beam polarization was periodically measured using a Møller polarimeter.

Each detector signal was integrated over the $\sim 25\mu\text{s}$ of the beam pulse and digitized along with the beam charge for that pulse. The ratio of integrated detector signal to integrated beam charge (normalized yield) was then corrected for background, beam polarization, and other systematic beam effects to give the experimental result for the parity-violating asymmetry.

For the SAMPLE kinematics, the parity-violating asymmetry for elastic scattering on the proton for the incident electron energy of 200 MeV can be written as

$$A_p = -5.56 + 1.54G_A^e(T = 1) + 3.37G_M^s \text{ ppm.} \quad (32)$$

(The isoscalar component of G_A^e is computed to be very small (15) and we have absorbed it into the leading constant term.) The SAMPLE measurement of this asymmetry (45) is

$$A_p = -5.61 \pm 0.67_{stat} \pm 0.88_{sys} \text{ ppm.} \quad (33)$$

Using the value of $G_A^e(T = 1) = -0.83 \pm 0.26$ from (15) results in the strange magnetic form factor

$$G_M^s(Q^2 = 0.1) = 0.37 \pm 0.20 \pm 0.26 \pm 0.07 \quad (34)$$

where the first uncertainty is statistical, followed by the estimated experimental systematic uncertainty and the last uncertainty is due to the axial corrections and electromagnetic form factors.

The asymmetry for quasielastic electron scattering deuterium for the SAMPLE kinematics and detector acceptance at 200 MeV is written

$$A_d = -7.06 + 1.66G_A^e(T = 1) + 0.72G_M^s \text{ ppm} \quad (35)$$

where the corrections for deuteron structure and other nuclear effects, including hadronic parity violation, have been included as discussed in (46). One should note that the deuteron asymmetry is more sensitive to the contribution from the isovector axial form factor $G_A^e(T = 1)$ than the proton asymmetry (47). The updated SAMPLE result for the deuterium asymmetry in quasielastic kinematics

is (48)

$$A_d = -6.79 \pm 0.64_{stat} \pm 0.55_{sys} \text{ ppm} . \quad (36)$$

A combined fit of the H and D data, assuming $G_E^s = 0$, allows a separation of G_M^s and $G_A^{T=1}$ and yields

$$G_M^s = 0.23 \pm 0.36_{stat} \pm 0.40_{sys} \quad (37)$$

$$G_A^e(T=1) = -0.53 \pm 0.57_{stat} \pm 0.50_{sys} , \quad (38)$$

which agrees well with the H result (Eq. 34) and also the theoretical prediction (15) for $G_A^e(T=1)$.

5.2 HAPPEX

The HAPPEX series of experiments were run in Hall A at Jefferson Lab, and made use of the High Resolution Spectrometers (50) to focus elastically scattered particles onto a total absorption shower counter in each focal plane whose signals were integrated over the 33 ms helicity period. The HRS suppressed background from inelastic scattering and low-energy secondaries.

The first generation HAPPEX experiment ran in 1998 and 1999 (17, 18, 49) at a kinematics $\langle \theta_{lab} \rangle = 12.3^\circ$ and $\langle Q^2 \rangle = 0.477 \text{ (GeV/c)}^2$ corresponding to the smallest angle and largest energy possible with the Hall A HRS spectrometers, which maximized the figure of merit for a first measurement.

In the 1998 run the experiment used a $I = 100\mu\text{A}$ beam with $P = 38\%$ polarization produced from a bulk GaAs crystal, while in the 1999 run HAPPEX-I became the first experiment to use a strained GaAs photocathode to measure a parity-violating asymmetry in fixed-target electron scattering. This improved the figure of merit P^2I with $P=70\%$ and $I=35\mu\text{A}$. (49)

During HAPPEX-I the Hall A Compton polarimeter (33) was commissioned and provided, for the first time, a continuous monitoring of the electron beam polarization with a total relative error from run-to-run of less than 2%. The Compton results were in good agreement with the Møller polarimeter in Hall A and a Mott polarimeter located in the 50 MeV region of the accelerator.

The HAPPEX-I physics asymmetry was found to be

$$A = -15.05 \pm 0.98_{stat} \pm 0.56_{sys} \text{ ppm} . \quad (39)$$

The precision of the result was sufficient to rule out several then-current theoretical estimates of strangeness effects at moderately high Q^2 where it was thought the effects might have been large (49).

Using this result, along with the calculated G_A^{Zp} and the known values of the proton and neutron form factors, the experiment determined the linear combination of strange form factors

$$G_E^s + 0.392G_M^s = 0.014 \pm 0.020 \pm 0.010 \quad (40)$$

where the first error is the total experimental error (statistical and systematic errors added in quadrature) and the second error is the error due to the “ordinary” electromagnetic form factors. One feature of the HAPPEX experiments is that they have negligible sensitivity to the axial form factors, whose effect is kinematically suppressed due to the very forward scattering angle.

The second generation HAPPEX experiments, HAPPEX-II and HAPPEX-Helium took data in 2004 and 2005 at a lower $Q^2 \sim 0.1 \text{ GeV}^2$, by utilizing superconducting septa magnets to allow the HRS to detect elastically scattered electrons at a scattering angle of 6° . The measurement on the ^4He target yielded an asymmetry of

$$A_{He} = +6.40 \pm 0.23_{stat} \pm 0.12_{sys} \text{ ppm}, \quad (41)$$

which tightly constrained the strange electric form factor to $G_E^s = 0.002 \pm 0.014 \pm 0.007$. The hydrogen data asymmetry

$$A_p = -1.58 \pm 0.12_{stat} \pm 0.04_{sys} \text{ ppm} \quad (42)$$

determined the form factor combination

$$G_E^s + 0.09G_M^s = 0.007 \pm 0.011_{stat} \pm 0.006_{sys}, \quad (43)$$

again, consistent with zero.

Subsequently, the HAPPEX-III experiment returned to higher Q^2 (0.62 GeV^2) with a data-taking run in 2009. This was motivated by indications of significant strange form-factor contributions at high ($> 0.4 \text{ GeV}^2$) Q^2 in results from the forward-angle phase of the G^0 experiment (see 5.3). HAPPEX-III capitalized on advancements in polarimetry, control of helicity-correlated beam fluctuations, and improved figure of merit compared to HAPPEX-I, leading to a precision asymmetry measurement

$$A_p = -23.80 \pm 0.78_{stat} \pm 0.36_{sys} \text{ ppm}, \quad (44)$$

yielding the form factor combination

$$G_E^s + 0.517G_M^s = 0.003 \pm 0.004_{stat} \pm 0.009_{sys}, \quad (45)$$

where the third error is due to electromagnetic form factors and radiative corrections. Again, the result is consistent with zero net strangeness contribution.

5.3 G^0

The G^0 experiment was performed in Hall C at Jefferson Lab. In this experiment the parity-violating asymmetry in elastic electron scattering from hydrogen and quasi-elastic electron scattering from deuterium was measured in the Q^2 range $0.1\text{-}1 \text{ (GeV}/c)^2$ in both forward and backward angle modes. By measuring three independent asymmetries, one at forward angles on liquid hydrogen and two at backward angles, one on liquid hydrogen and one on liquid deuterium, a complete separation of the strange vector form factors of the nucleon (G_M^s, G_E^s) and the isovector axial form factor ($G_A^e(T=1)$) was possible. In the forward angle mode the particle detected was the recoil proton, while in the backward angle mode the particle detected was the scattered electron. The experiment ran in forward angle mode during the period 2002-5 and in backward angle mode during 2006-7.

The G^0 experiment employed a large-acceptance superconducting toroidal spectrometer with eight coils and eight sets of particle detectors providing excellent azimuthal symmetry about the beam axis. In forward angle mode, the recoiling protons were detected using 16 pairs of plastic scintillation detectors in each

octant. Each detector pair (one behind the other) selected coincident events to reduce accidental backgrounds. The incident beam of 3 GeV electrons was delivered in short (~ 100 ps) pulses at 31 MHz to allow a 32 ns time of flight window for detection of the recoil protons. Custom time-encoding electronics enabled measuring the protons as a function of time of flight in pulse counting mode. At the larger $Q^2 \geq 0.3$ (GeV/c)², large positive asymmetries due to hyperon decay backgrounds necessitated careful treatment and correction to extract the much smaller negative asymmetries due to parity violation in elastic scattering. The forward angle G0 measurements (25) enable a simultaneous determination of the quantity $G_E^s + \eta G_M^s$ over the Q^2 range 0.1-1 (GeV/c)², where $\eta \equiv \tau G_M^\gamma / \epsilon G_E^\gamma$. The results are shown in Fig. 6.

The G0 backward angle results were obtained using incident beams at 359 MeV and 684 MeV. The orientation of the toroidal spectrometer was reversed to facilitate measurement of scattered electrons near 110° with respect to the incident beam direction. The scintillation detectors (called focal plane detectors, FPD) were supplemented with additional scintillators near the exit of the magnet (cryostat exit detectors, CED) and aerogel threshold Cerenkov counters (pion threshold 570 MeV) to reject pions. The backward angle results (hydrogen and deuterium) were combined with the forward angle measurements to yield values of G_E^s , G_M^s , and $G_A^e(T=1)$ (29) at two values of Q^2 (0.221 and 0.628 GeV²) as shown in Fig. 7.

5.4 PVA4

The PVA4 collaboration at the MAMI microtron adopted a counting-mode approach, with a highly segmented calorimeter along with custom fast electronics. No magnetic spectrometer is used; the signal is separated from backgrounds using the energy deposition in the calorimeter. The calorimeter is an azimuthally symmetric array of 1022 PbF2 crystal, in seven rings covering scattered electron angles from either 30° to 40° (forward configuration) or 140° to 150° (backward configuration), acting as a total-absorption Cerenkov detector (51). The spectrum of energy deposited above a hardware threshold in clusters of 9 crystals is histogrammed using pipelined fast digitizer and the energy histograms are stored for each helicity state. The beam current is typically 20 μ A, with a polarization of 80%, and the helicity state is selected every 20 ms.

The first PVA4 measurement was in a forward-angle configuration, with a liquid hydrogen target; the measured asymmetry is sensitive to a linear combination of G_E^s and G_M^s . The beam energy was 855 MeV yielding a $Q^2 = 0.230$ (GeV/c)². For this initial measurement, only half of the 1022 detector channels were instrumented. The measured asymmetry was (52).

$$A_p(Q^2 = 0.230) = -5.44 \pm 0.54_{stat} \pm 0.26_{sys} \text{ ppm} . \quad (46)$$

This asymmetry implies a value for the linear combination of the strange form factors of

$$(G_E^s + 0.225G_M^s)(Q^2 = 0.230) = 0.039 \pm 0.034. \quad (47)$$

The second PVA4 forward-angle measurement made use of the fully instrumented detector. Data were taken on liquid hydrogen with a beam energy of 570

MeV, at $Q^2 = 0.108$ (GeV/c)², and yielded an asymmetry of

$$A_p(Q^2 = 0.108) = -1.36 \pm 0.29_{stat} \pm 0.13_{sys} \text{ ppm}, \quad (48)$$

which implies the value of

$$(G_E^s + 0.106G_M^s)(Q^2 = 0.108) = 0.071 \pm 0.036 \quad (49)$$

for the linear combination (53). This later result represents a nearly 2σ deviation from zero.

After these two forward-angle measurements, the PVA4 apparatus was turned around and modified for a series of backward-angle measurements. Added to the detector was a double-ring of 72 scintillator counters, each of which cover 14 of the PbF₂ detectors. These are used for electron tagging in order to suppress the copious background of photons arising from π^0 decay.

The first back-angle measurement on hydrogen was at 315 MeV beam energy and Q^2 of 0.230 (GeV/c)², to match the Q^2 of one of the forward-angle points. The result was (54)

$$A_p(Q^2 = 0.230) = -17.23 \pm 0.82_{stat} \pm 0.89_{sys} \text{ ppm}. \quad (50)$$

The measured asymmetry implies a value for the linear combination of the strange form factors of

$$(G_M^s + 0.26G_E^s)(Q^2 = 0.230) = -0.12 \pm 0.11_{stat} \pm 0.11_{sys}. \quad (51)$$

Data were also taken at the same kinematics with a liquid deuterium target; results are expected soon (55). The MAMI accelerator has undergone an energy upgrade to allow beam energies up to 1.5 GeV, opening up a wider range of Q^2 for the PVA4 experiment. The collaboration has since moved the detector back into its forward scattering configuration (55), and taken data at $Q^2 = 0.63$ (GeV/c)², which matches the kinematics of both the HAPPEX-III experiment and the higher Q^2 point at backward angle from G0.

6 CONCLUSIONS

During the last decade there has been a substantial international effort to perform measurements of parity-violating asymmetries in elastic electron scattering from nucleons. The primary aim of this program has been to constrain the strange quark-antiquark contributions to the nucleon electroweak form factors, G_E^s and G_M^s , as a function of momentum transfer Q^2 . The experiments have made great progress in advancing the techniques required to perform reliable and precise measurements that enable extraction of the form factors. Substantial theoretical effort has provided confidence in the radiative corrections and the degree of uncertainty associated with contributions to the axial form factor G_A^e . As a result, we now have a rather clear picture that has emerged from this body of work.

In general, a convincing signal for a significant strange quark-antiquark effect in the vector form factors has not been obtained from these measurements. The various experimental results at different kinematics all seem to support this general conclusion. In fact, the results are remarkably consistent with this conclusion despite the difficulty of these very challenging experiments.

At the lowest momentum transfers ($Q^2 \sim 0.1 \text{ (GeV/c)}^2$), there have been global fits performed to the body of experimental data in this kinematic region (56, 57). These fits illustrate the consistency of the data and reinforce the conclusion that the strange vector form factors are quite small (compared to many model predictions) at this low Q^2 . Fig. 9 shows the result of the most recent of these global fits (56). As a result, one can now conclude that, with 95% confidence, strange quarks contribute less than 5% of the mean-square charge radius and less than 6% of the magnetic moment of the proton.

It is fair to say that these results are rather surprising in light of the guidance from many models of nucleon structure that predicted substantial strange quark effects at low Q^2 . The result also seems to be at variance with the notion that baryon-meson fluctuations are a significant aspect of nucleon structure as one would infer from the $\bar{d} - \bar{u}$ asymmetry observed in Drell-Yan production and the success of many meson cloud models of the nucleon. More recently, there have been results based on Lattice QCD calculations (7, 8, 9) that seem to support the very small values of the strange form factors indicated by the experiments. It is certainly gratifying that these calculations are consistent with experiment. Nevertheless, they do not provide much insight as to *why* the strange quark contributions are suppressed in these quantities. In the end, one has to admit that we have certainly learned something quite significant about nucleon structure from this program but that a deeper understanding of this phenomenon is still lacking.

On the practical side, the conclusion that strange form factors are constrained to be small combined with the development of the experimental techniques for parity-violating electron scattering experiments has motivated new experiments to perform precision tests of the standard electroweak model in parity-violating electron scattering. In particular, the experimental program reviewed here, and the constraint on the strange electric form factor of the proton G_E^s , provides a quantitative basis for assessing the utility of low Q^2 measurements of parity-violating electron scattering to provide precise new information on the running of the weak mixing angle θ_W (58). For example, the Qweak experiment at Jefferson Lab (59, 60) is presently underway and expects to provide a measurement of $\sin^2 \theta_W$ to about 0.24% precision. Such a measurement would herald a new era of precision tests of the standard model that could reveal effects associated with new physics at the TeV scale.

7 ACKNOWLEDGEMENTS

This work was supported in part by DOE contract DE-AC05-06OR23177, under which Jefferson Science Associates, LLC, operates the Thomas Jefferson National Accelerator Facility, and by NSF grants PHY-0758068 and PHY-1068667. We also thank our colleagues in the SAMPLE, HAPPEX, G0, and PVA4 collaborations for many fruitful discussions and interactions.

8 NUMBERED LITERATURE CITED

LITERATURE CITED

1. Kaplan D and Manohar A, 1988. *Nucl. Phys.* B310:527
2. McKeown RD, 1989. *Phys. Lett.* B219:140

3. Beck DH, 1989. *Phys. Rev. D* 39:3248
4. Martin AD, Stirling WJ, Thorne RS, and Watt G 2009. *Eur. Phys. J. C* 63: 189.
5. Nakamura K, et al. (Particle Data Group) 2010. *J. Phys. G* 37: 075021
6. Beck DH, and Holstein BR, 2001. *Int. J. Mod. Phys. E* 10:1
7. Leinweber DB, et al., 2005. *Phys. Rev. Lett.* 94:212001
8. Leinweber DB, et al., 2006. *Phys. Rev. Lett.* 97:022001
9. Doi T, et al., 2009. *Phys. Rev. D* 80:094503
10. Erler J, Kurylov, A and Ramsey-Musolf, MJ, 2003. *Phys. Rev. D.* 68:016006
11. Erler J, and Ramsey-Musolf MJ, 2005. *Phys Rev D* 72:073003
12. Budd H, Bodek A, and Arrington J, 2003. arXiv:hep-ex/0308005
13. Filippone BW, and Ji XD, 2001. *Adv. Nucl. Phys.* 26:1
14. Adams D, et al. [Spin Muon Collaboration (SMC)], 1997. *Phys. Rev. D* 56:5330
15. Zhu S, et al., 2000. *Phys. Rev. D* 62:033008
16. Prescott CY, et al. 1978. *Phys. Lett.* B77:347
17. Aniol KA, et al. 1999. *Phys. Rev. Lett.* 82: 1096
18. Aniol KA, et al. 2001. *Phys. Lett.* B509: 211
19. Nakanishi T, et al. 1991. *Phys. Lett.* A158:345
20. Maruyama T, et al. 1991. *Phys. Rev. Lett.* 66:2376
21. Maruyama T, et al. 2004. *Appl. Phys. Lett.* 85:2640
22. Ahmed Z, et al. 2011. arXiv:1107.0913
23. Humensky, TB, et al. 2004. *Nucl. Instrum. Methods Phys. Res. A* 521: 261
24. Paschke KD, 2007. *Eur. Phys. J A* 32, 549.
25. Armstrong DS, et al. 2005. *Phys. Rev. Lett.* 95:092001
26. Aniol KA, et al. 2006. *Phys. Lett.* B635:275
27. Aniol KA, et al. 2006. *Phys. Rev. Lett.* 96:022003
28. Acha A, et al. 2007. *Phys. Rev. Lett.* 98:032301
29. Androic D, et al. 2010. *Phys. Rev. Lett.* 104: 012001
30. Averett T, Jones CS, McKeown RD, and Pitt M 1999. *Nucl. Instrum. Methods Phys. Res. A* 438: 246
31. Weinrich C 2005. *Eur. Phys. J. A* 24S2:129
32. Beise EJ, Pitt ML, and Spayde DT, 2005. *Prog. Part. Nucl. Phys.* 54:289
33. Baylac M, et al., 2002. *Phys. Lett. B* 539:8
34. Neyret D, et al., 2000. *Nucl. Instrum. Methods Phys. Res. A* 443:231
35. Jorda JP, et al., 1998. *Nucl. Instrum. Methods Phys. Res. A* 412:1
36. Falletto N, et al., 2001. *Nucl. Instrum. Methods Phys. Res. A* 459:412
37. Diefenbach J, 2011. *Hyperfine Int.* 200:41
38. Price JS, et al., 1999. *Proc. SPIN98, Protvino, Russia, 1998, World Scientific, Singapore*
39. Glamazdin AV, et al., 1999. *Fizika B* 8:91
40. Hauger M, et al., 2001. *Nucl. Instrum. Methods Phys. Res. A* 462:382
41. Bartsch P, 2001. PhD thesis (unpublished), U. Mainz
42. Beise E, et al., 1996. *Nucl. Instrum. Methods Phys. Res. A* A378:383
43. Covrig S, et al., 2005. *Nucl. Instrum. Methods Phys. Res. A.* 551:218
44. Altarev I, et al., 2006. *Nucl. Instrum. Methods Phys. Res. A* 640:58
45. Spayde DT, et al. 2000. *Phys. Rev. Lett.* 84:1106
46. Sciavilla R, Carlson J, and Paris MW, 2004. *Phys. Rev. C* 70:044007
47. Beise EJ, and McKeown RD, 1991. *Comment Nucl. Part. Phys.* 20:105
48. Ito TM, et al. 2004. *Phys. Rev. Lett.* 92:102003

49. Aniol KA, et al. 2004. *Phys. Rev. C* 59:065501
50. Alcorn J, et al. 2004. *Nucl. Instrum. Methods Phys. Res. A* 522:294
51. Baunack S, et al. 2011. *Nucl. Instrum. Methods Phys. Res. A* 640: 58
52. Maas FE, et al. 2004. *Phys. Rev. Lett.* 93:022002
53. Maas FE, et al. 2005. *Phys. Rev. Lett.* 94:152001
54. Baunack S, et al. 2009. *Phys. Rev. Lett.* 102:151803
55. Baunack S, 2011. *Hyperfine Int.* 200:13
56. Liu J, McKeown RD, and Ramsey-Musolf MJ, 2007. *Phys. Rev. C.* 76:025202
57. Young RD, Roche J, Carlini RD, and Thomas AW, 2006. *Phys. Rev. Lett.* 97:102002
58. Young RD, Carlini RD, Thomas AW, and Roche J, 2007. *Phys. Rev. Lett.* 99:122003
59. Jefferson Lab proposal E08-016.
60. van Oers WTH, 2008. *Nucl. Phys. A* 805:329.

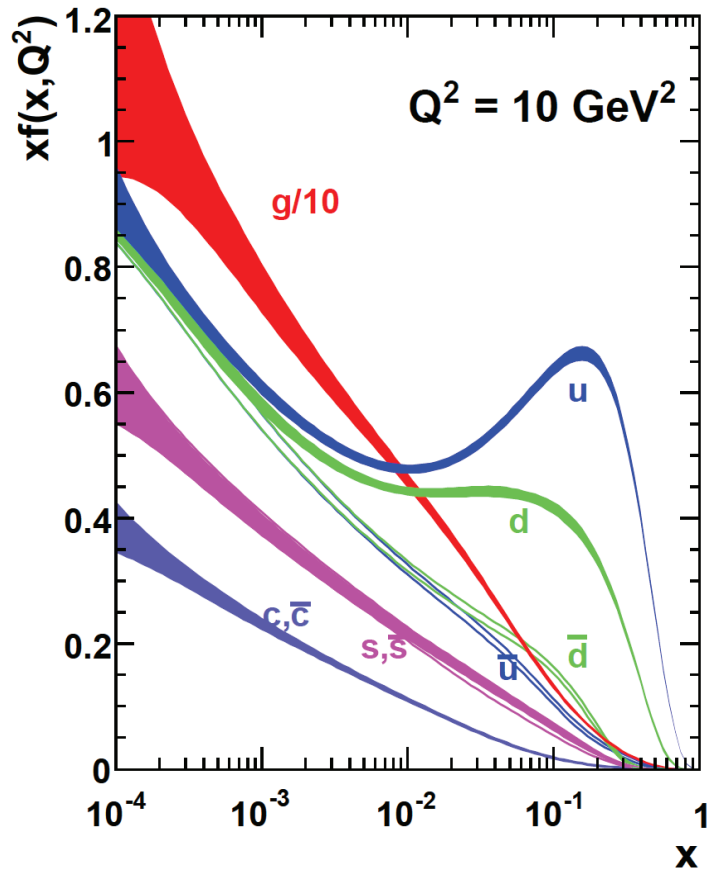


Figure 1: The results of a global fit (4) for the quark, antiquark, and gluon parton distribution functions as a function of the momentum fraction x , at $Q^2 = 10 \text{ GeV}^2$. Note that the PDF's $f(x)$ are multiplied by x to suppress the large rise at low x in the plot, and that the gluon distribution is divided by 10 for display purposes.

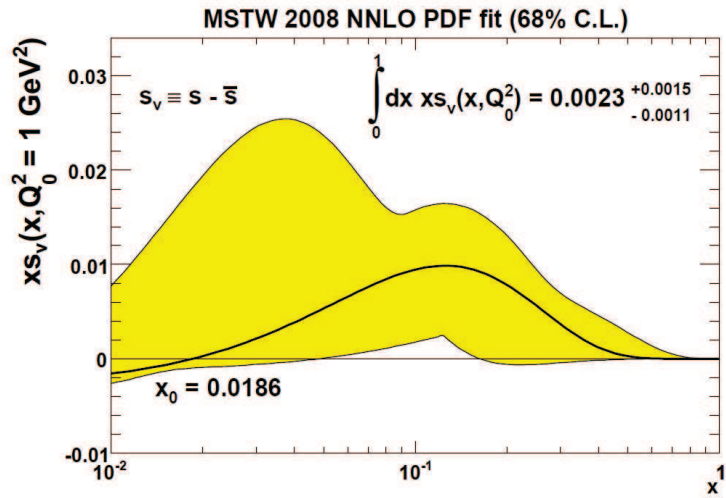


Figure 2: The results of the recent global fit (4) for the difference $s(x) - \bar{s}(x)$.



Figure 3: The amplitudes relevant to parity-violating electron scattering. The dominant parity-violating effects arise from the interference of these two amplitudes.

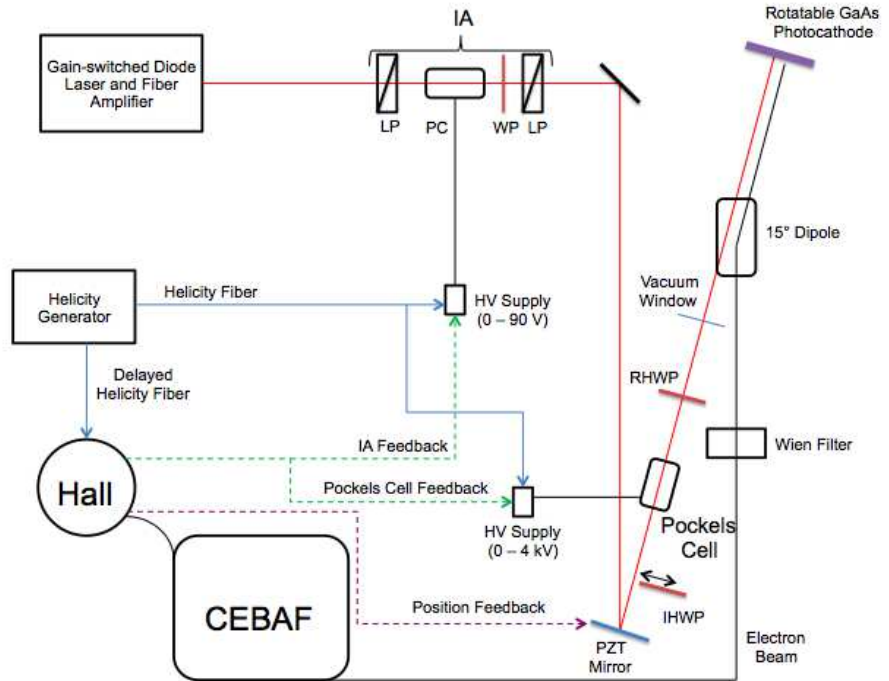


Figure 4: Schematic of the polarized injector source at Jefferson Lab. The laser light passes through an intensity attenuator system (IA) (see text) and is directed by a PZT-mirror to the primary helicity-control Pockels cell. An insertable half-wave plate (IHWP) can be placed in the optical path (see text). Passing through a rotatable half-wave plate (RHWP) the light is directed onto the photocathode. The emitted electron beam passes through a Wien filter, to adjust the spatial orientation of the electron spin, and is injected into the CEBAF accelerator. The helicity generator signal is sent via fibre optics both to the high-voltage source for the Pockels cell and to the experimental data acquisition system. Helicity-correlated variations in the beam intensity and position are monitored in the experimental Hall and can generate feedback signals to the source as outlined in the text.

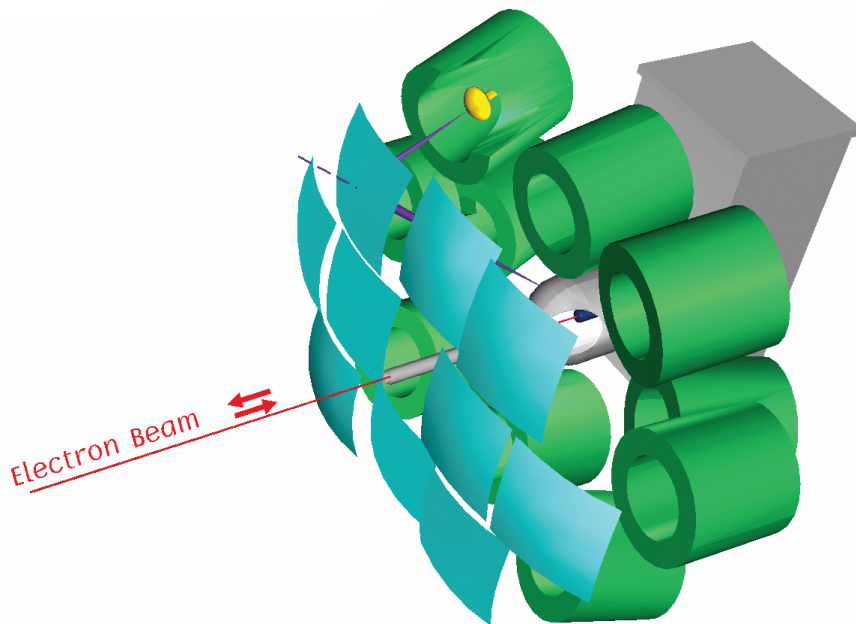


Figure 5: Illustration showing the geometry of the SAMPLE target and detector system. The electron beam is incident from the left. The electrons scattered at backward angles emitted Cerenkov light in the air, which was reflected by 10 mirrors onto ten 8-inch photomultiplier tubes. The photomultipliers were mounted inside cylindrical cast lead shields to reduce background.

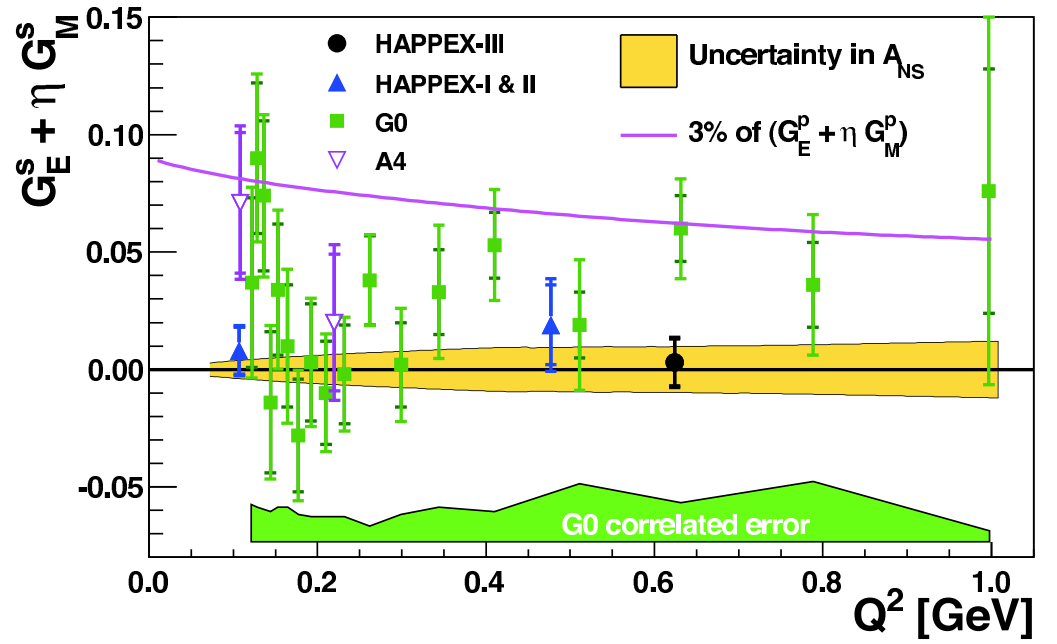


Figure 6: Strange quark vector form factor results from all forward-angle scattering measurements on the proton as a function of Q^2 . For the G^0 results (25), the inner error bars are statistical and the outer are point-to-point systematics, with the correlated systematic error shown as a green band. The yellow band shows the uncertainty in the predicted asymmetries in the absence of strangeness effects, due to knowledge of the electromagnetic and axial form factors. For reference, the solid curve shows a 3% contribution to the comparable linear combination of proton form factors.

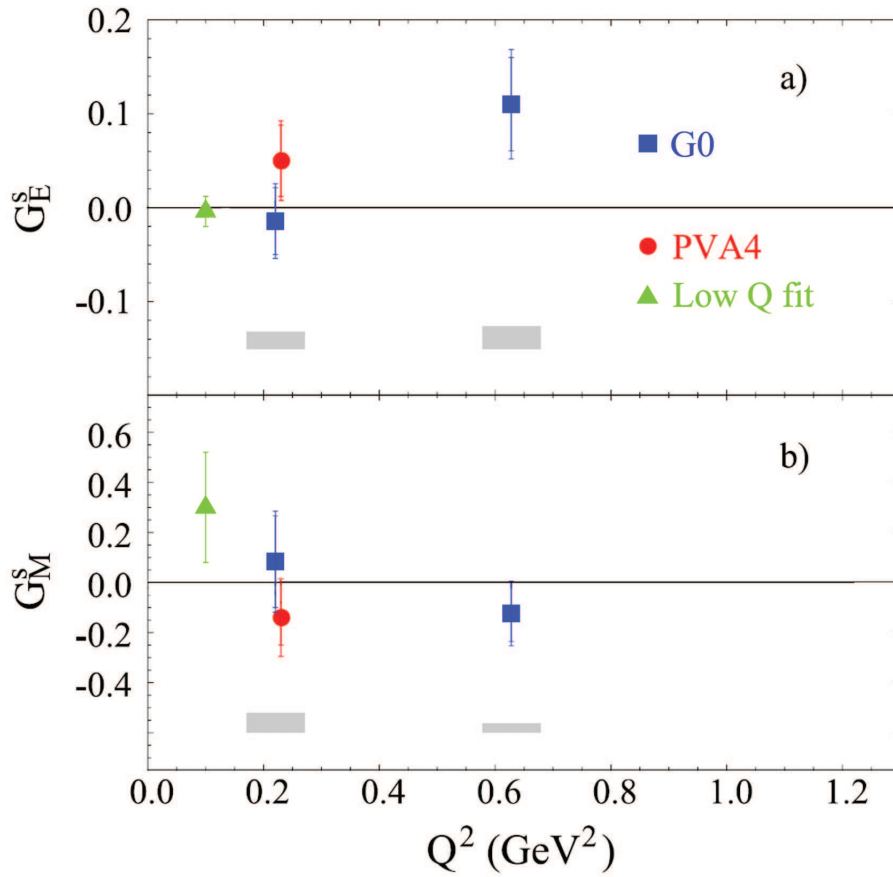


Figure 7: Results for the strange vector form factors extracted from combining the forward and backward-angle G0 experiments on hydrogen and deuterium (29); also shown are the results from PVA4 at $Q^2 = 0.23 \text{ GeV}^2$ (52, 54), and a global fit (56) to world data at $Q^2 = 0.1 \text{ GeV}^2$. The grey bands are correlated systematic errors for the G0 data.

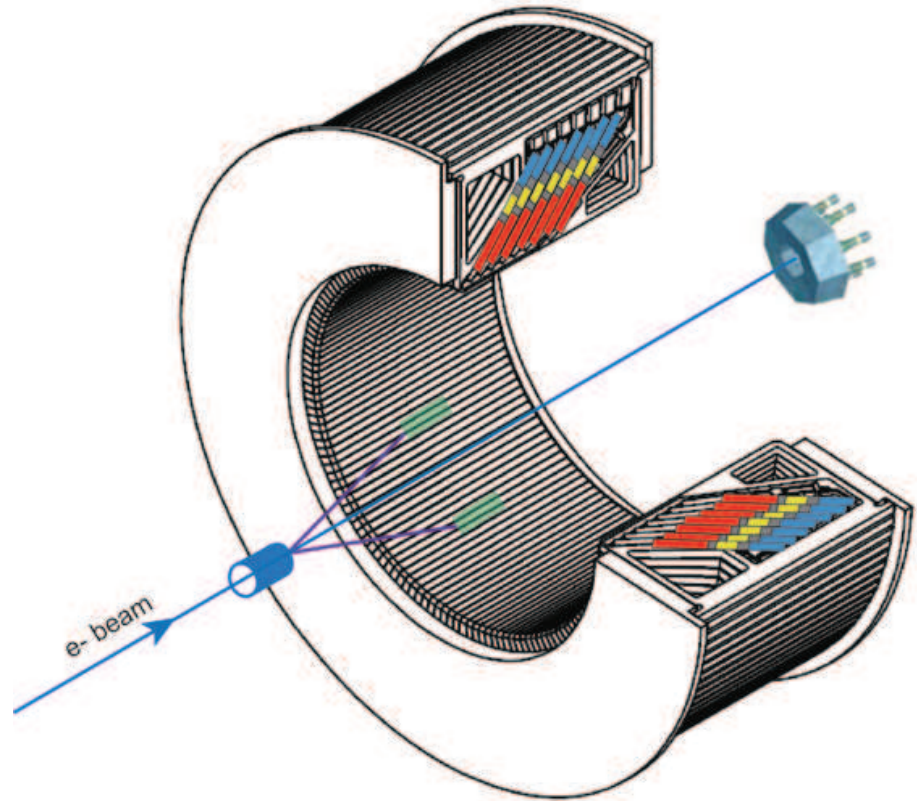


Figure 8: Layout of the PVA4 detector. The electron beam is incident from the left; scattered electrons are detected in the projective-geometry PbF₂ calorimeter, consisting of 7 rings of crystals in 146 rows. Beam intensity fluctuations are monitored using a water Cerenkov luminosity monitor system detecting small-angle scattering, shown on the right.

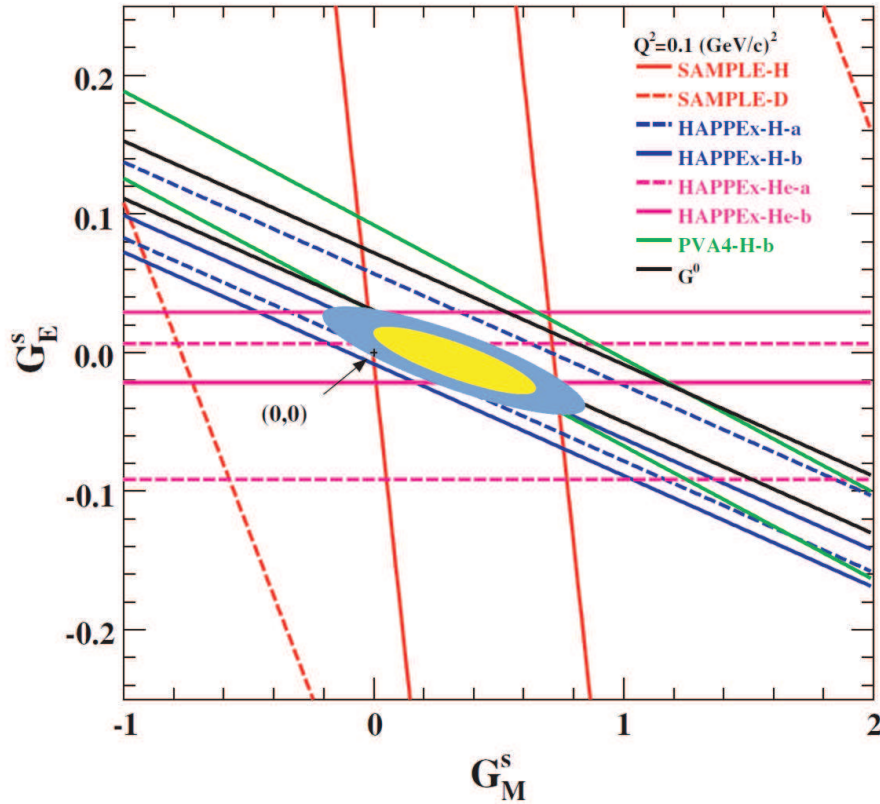


Figure 9: The world data constraints on (G_E^s, G_M^s) at $Q^2 = 0.1(\text{GeV}/c)^2$. The form factors of Kelly are used. Different bands in the plot represent SAMPLE-H (45) (solid red), SAMPLE-D (48) (dashed red), HAPPEX-H-a (26) (dashed blue), HAPPEX-H-b (28) (solid blue), HAPPEX-He-a (27) (dashed pink), HAPPEX-He-b (28) (solid pink), PVA4-H-b (53) (solid green), and the lowest three Q^2 bins in G^0 forward angle (25) (solid black). The yellow and gray blue (dark) ellipses represent 68.27% ($\Delta\chi^2 = 2.3$) and 95% ($\Delta\chi^2 = 5.99$) confidence contours around the point of maximum likelihood at $(G_E^s = 0.006, G_M^s = 0.33)$. The black cross represents $G_E^s = G_M^s = 0$.